

Article

Comparison of SLSTR Thermal Emissive Bands Clear-Sky Measurements with Those of Geostationary Imagers

Bingkun Luo *  and Peter J. Minnett 

Rosenstiel School of Marine and Atmospheric Science, University of Miami, 4600 Rickenbacker Causeway, Miami, FL 33149, USA; pminnett@rsmas.miami.edu

* Correspondence: LBK@rsmas.miami.edu

Received: 25 August 2020; Accepted: 7 October 2020; Published: 9 October 2020



Abstract: The Sentinel-3 series satellites belong to the European Earth Observation satellite missions for supporting oceanography, land, and atmospheric studies. The Sea and Land Surface Temperature Radiometer (SLSTR) onboard the Sentinel-3 satellites was designed to provide a significant improvement in remote sensing of skin sea surface temperature (SST_{skin}). The successful application of SLSTR-derived SST_{skin} fields depends on their accuracies. Based on sensor-dependent radiative transfer model simulations, geostationary Geostationary Operational Environmental Satellite (GOES-16) Advanced Baseline Imagers (ABI) and Meteosat Second Generation (MSG-4) Spinning Enhanced Visible and Infrared Imager (SEVIRI) brightness temperatures (BT) have been transformed to SLSTR equivalents to permit comparisons at the pixel level in three ocean regions. The results show the averaged BT differences are on the order of 0.1 K and the existence of small biases between them are likely due to the uncertainties in cloud masking, satellite view angle, solar azimuth angle, and reflected solar light. This study demonstrates the feasibility of combining SST_{skin} retrievals from SLSTR with those of ABI and SEVIRI.

Keywords: SLSTR; evaluation; thermal bands; ABI; SEVIRI

1. Introduction

Skin sea surface temperature (SST_{skin}) is one of the critical variables in the climate system, indicating air–sea interaction patterns near the upper ocean skin layer [1]. The infrared radiometers on earth observation satellites, in both geostationary and polar orbits, have provided retrievals of sea surface temperature (SST) for a half-century [2]. Our choice of satellite radiometers for this analysis was guided by the desire to include one on a polar-orbiting satellite of recent design but with a long planned deployment sequence, a new radiometer type on geostationary satellites again with a long planned deployment duration, and an older radiometer design in geostationary orbit of a type that has been producing data for many years. Thus, the study has relevance not only for the present, but also for the past and future.

The new generation of visible and infrared imaging radiometers, the Sea and Land Surface Temperature Radiometer (SLSTR) onboard Copernicus Sentinel-3A and Sentinel-3B satellites, provide global operational measurements that can be used to derive SST_{skin} , land surface temperature, fire radiative power, aerosol optical depth, etc. [3–5]. The SLSTRs are the fourth and fifth along-track scanning radiometers and are based on the prior along-track scanning radiometers (ATSR; [6]) and advanced ATSR (AATSR; [7]), which have provided valuable measurements to study the Earth's climate system and improve weather forecasting and ocean studies [3,4].

SLSTR was designed to achieve the scientific objective of a mean temporal accuracy of 0.1 K for SST_{skin} products [4]. However, this potential will not be realized without the accurate measurements of top-of-atmosphere radiances. Absolute calibration should be applied to the radiometer, SLSTR

radiometric pre-launch calibration is determined at the Rutherford Appleton Laboratory in the United Kingdom (UK) [8,9]. The SLSTR onboard radiometric calibration of the infrared channels is based on two blackbodies with different temperatures (265K and 302K) [8].

With the significant improvements on prior sensors on satellites in geostationary orbits, the new generation of sensors, such as the Advanced Baseline Imager (ABI; [10]) onboard the United States (US) Geostationary Operational Environmental Satellite (GOES) series along with the relatively old sensor Spinning Enhanced Visible and InfraRed Imager (SEVIRI; [11]) onboard the fourth satellite in Meteorat Second Generation (MSG-4), can sample the low- and mid-latitude regions of the Earth's surface and atmosphere and provide valuable data for comparison SLSTR brightness temperatures (BT) in this study.

Sensor-to-sensor comparison can be used to provide assessment on many newly launched sensors. The previous solar reflective band comparisons between the Advanced Himawari Imager (AHI; [12]) and the Visible Infrared Imaging Radiometer Suite (VIIRS; [13]) by Yu and Wu [14] confirmed the linear relationships between them using collocated pairs. The collocated deep convective cloud data have a small difference in the near-infrared bands. Liang, et al. [15] compared measurements and simulations of the AHI, VIIRS and MODerate-resolution Imaging Spectroradiometers (MODIS; [16]) for clear-sky radiances above the sea surface and found the biases in the sensor radiances minus model simulated radiances are relatively stable. Li, et al. [17] have reported a comparison of measurements of MODIS and VIIRS thermal emissive bands using Atmospheric Infrared Sounder (AIRS) hyperspectral radiances convolved with the relative spectral response functions of the MODIS and VIIRS bands, they found the BTs agree relatively well with each other, the differences being within 0.2K. Many other investigators also use this approach to conduct comparisons between various sensors [17–19]. We use conversion functions derived by radiative transfer model simulations to convert the BTs retrieved by geostationary satellite radiometers into SLSTR equivalent versions to perform the analysis reported here. This method has been used by Yu and Wu [14], NASA Langley spectral band difference adjustment [20] and Wu, et al. [21] and others, and found to be useful.

SLSTR, ABI, and SEVIRI provide capabilities for deriving SST_{skin} from the clear sky “atmospheric windows” of wavelengths 3.5–4.1 μm and 8.5–12 μm spectral intervals (which are called thermal emissive bands here). Among the SLSTR, nine spectral channels in the 0.554–12.022 μm spectral range, S7 ($\lambda = 3.74 \mu m$), S8 ($\lambda = 10.95 \mu m$), and S9 ($\lambda = 12.00 \mu m$), can be used for deriving SST_{skin} [22]. For ABI and SEVIRI, the additional bands near $\lambda = 8.5$ – $8.7 \mu m$ are also useful for SST_{skin} retrieval [23–25], as well as in the cloud mask used to eliminate measurements containing radiance emitted or modified by clouds [26]. SST_{skin} derived from measurements in these thermal bands have provided long time-series for various studies [2], the stability of measurements in these bands must be continuously evaluated, especially when they are used to assess the rapidly environmental changes.

This study focused on the preliminary inter-comparison of the new generation of SLSTR radiometers with geostationary radiometers ABI and SEVIRI, in which the performance of the thermal emissive bands were compared. We organize this paper as follows: an overview of the different satellite data is introduced in Section 2. The inter-comparisons between SLSTR and ABI, as well as SLSTR and SEVIR, in three regions, are discussed in Section 3. The reasons for the uncertainties are also introduced in Section 3. Section 4 gives the conclusion of this study.

2. Methods and Materials

2.1. Overview of the Satellite Data

The datasets used in this study include those from radiometers on Sentinel-3A, MSG-4, and GOES-16 satellites are all freely accessible from data servers. Here, we briefly describe the characteristics of the satellite radiometers and their thermal emissive bands that are used to derive SST_{skin} . Relative spectral response functions of SLSTR and the corresponding ABI and SEVIRI channels are given in Figure 1 and Table 1. The gray line in Figure 1 is the atmospheric transmission spectrum for

vertical propagation through a standard atmosphere, the spectral response functions of these thermal emissive channels are similar.

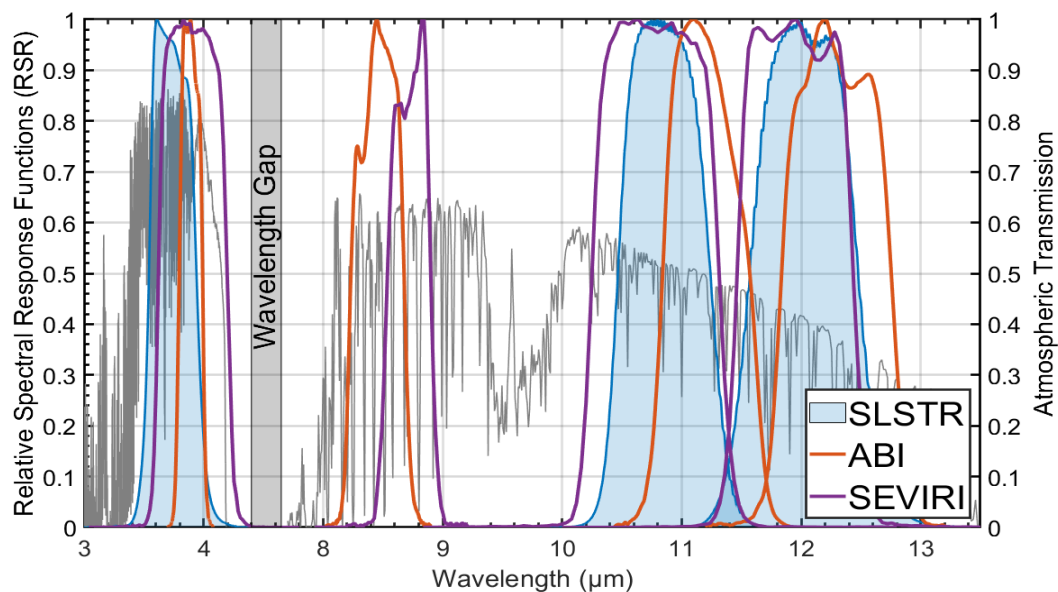


Figure 1. Relative spectral response function of the Sea and Land Surface Temperature Radiometer (SLSTR), with those of Advanced Baseline Imagers (ABI) and Spinning Enhanced Visible and Infrared Imager (SEVIRI) thermal bands around wavelengths of 3.7 μm , 8.9 μm , 11 μm and 12 μm . Data are from National Oceanic and Atmospheric Administration Center for Satellite Applications and Research (STAR) National Calibration Center for Visible Infrared Imaging Radiometer Suite (VIIRS)/ABI, from the European Space Agency (ESA) Sentinels Hub for SLSTR and SEVIRI. The gray line is the atmospheric transmission spectrum for vertical propagation through a standard atmosphere.

Table 1. Spectral bands of the SLSTR and geostationary satellite radiometers ABI and SEVIRI. All these bands are usually referred to as thermal emissive bands. Only those with a sea surface temperature (SST) capability are shown.

Band	Band	Center Wavelength (μm)	Band	Center Wavelength (μm)	Band	Center Wavelength (μm)
	GOES-ABI		MSG-4 SEVIRI		Sentinel-3A SLSTR	
IR038	7	3.90	4	3.90	S7	3.74
IR087	11	8.50	7	8.70	-	-
IR112	14	11.20	9	10.80	S8	10.95
IR123	15	12.30	10	12.00	S9	12.00

The ability to retrieve the SST_{skin} by making atmospheric corrections is based on different atmospheric transmissions at different infrared wavelengths. The measurements are usually taken in spectral regions with wavelengths from $\sim 3.5 \mu\text{m}$ to $\sim 4.1 \mu\text{m}$ and $\sim 10 \mu\text{m}$ to $\sim 13 \mu\text{m}$, where the atmosphere is quite transparent, with variations in clear-sky transmission caused primarily by water vapor, which in itself is highly variable. The widely used SST_{skin} retrieval algorithm, the non-linear SST (NLSST; [27]), is based on the atmospheric transmission window near the IR112 and IR123 bands (Table 1), with other dependences on satellite zenith angle, first-guess SST, coefficient set for latitude bands and month of year [2,28]. The IR038 band near the 3.7–3.9 μm interval can be used to retrieve nighttime SST_{skin} and correct dust aerosol effect [29–31]. Both ABI and SEVIRI are spectrally matched to three SLSTR bands, S7, S8, and S9, respectively. Additionally, ABI and SEVIRI have an IR086 band near 8.5–8.7 μm for deriving SST_{skin} . However, the SLSTR does not include a similar IR086 band in their SST_{skin} retrievals. For this reason, we only consider comparisons of the bands near the SLSTR S7 ($\lambda = 3.74 \mu\text{m}$), S8 ($\lambda = 10.95 \mu\text{m}$), and S9 ($\lambda = 12.00 \mu\text{m}$) spectral ranges in this study.

Figure 2 shows the one-day track of Sentinel-3A as well as the coverage of the GOES-16 and MSG geostationary meteorological satellites that will be used in this study. Table 2 gives the temporal and spatial resolutions of the three satellite retrievals. Details of each radiometer are given in Sections 2.2–2.4.

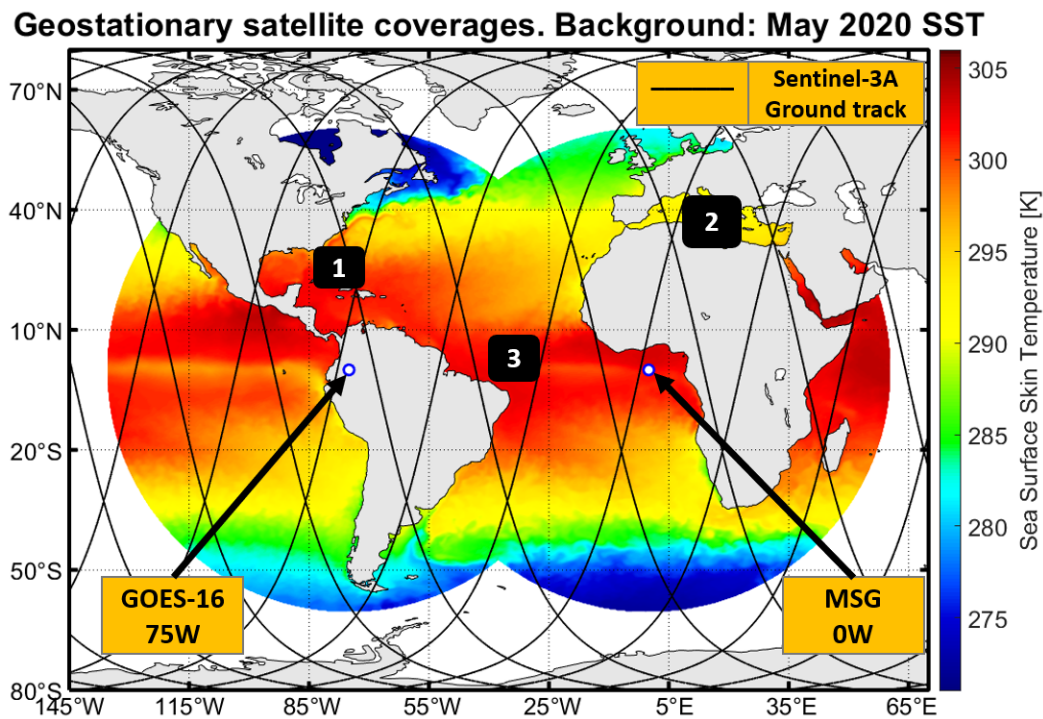


Figure 2. The Sentinel-3A one-day ground tracks along with the coverage areas of the two geostationary meteorological satellites currently in operation and are used in this study. May 2020 monthly mean SST is the background. Three black rectangles indicate the research areas in this study, the numbers correspond to the three parts in Section 4.

Table 2. Characters of each satellite product.

Satellite	Available from	Temporal Resolution	Spatial Resolution
Sentinel-3A SLSTR	EUMETSAT Copernicus Online Data Access (CODA)	every 3 min for Level-1B data	1 km
GOES-ABI	NOAA Amazon Web Services (AWS) Data Centre	every 10 min	1 km
MSG-4 SEVIRI	EUMETSAT Data Centre	every 15 min	3 km

2.2. SLSTR Data

The European Copernicus Sentinel-3A was launched in February 2016 into a polar orbit with descending equator crossing time at 10:00 AM. SLSTR is one of the key instruments for the European Copernicus Sentinel observational system. Unlike the MODIS and VIIRS, which are broad-swath linear-scanners with an atmospheric correction based on the differential atmospheric effects at different wavelengths, the SLSTR onboard Sentinel-3A and Sentinel-3B satellites includes dual view scan systems taking measurements through different atmospheric paths, providing direct measurements of the atmospheric effect, but at the cost of narrower swaths of 740 km. The SLSTR also has a wider nadir view with 1400 km swath. The SLSTRs can provide accurate SST_{skin} derived by radiative transfer model simulated top-of-atmosphere BTs [22,32]. Since the $3.74 \mu m$ band can be contaminated during daytime

by solar radiation, the SLSTR SST_{skin} is selected from a selection of four algorithms depending on single-view, dual-view, daytime, and nighttime. An initial assessment of the Sentinel-3A SLSTR SST_{skin} accuracy determined by comparisons with measurements of the ship-borne Marine-Atmospheric Emitted Radiance Interferometer (M-AERI; [33]) indicates a median discrepancy of -0.098 K with a robust standard deviation of 0.296 K [3].

2.3. ABI Data

The National Oceanic and Atmospheric Administration (NOAA) geostationary satellite GOES-16, located above 75.2° W, began operation on December 16th, 2017 [10]. ABI has 16 spectral channels, including six visible and near-infrared channels and ten in the infrared. The ABI uses an internal blackbody target and deep space for calibrating the thermal bands. The ABI has improved performance with regard to radiometric calibration accuracy and image navigation/registration compared to prior instruments, it provides full-disk imagery every 10 minutes and the nearest in time Level 2 Cloud and Moisture Imagery Full Disk (CMIPF) data are used to compare with the corresponding SLSTR scenes. The ABI CMIPF files were downloaded from the NOAA data project on Amazon Web Services (AWS) at no cost. The ABI Advanced Clear Sky Processor for Ocean (ACSPO) cloud mask [34] was also used in this study to identify and remove the cloudy pixels.

2.4. SEVIRI Data

Located in geostationary orbit at 0° longitude, SEVIRI onboard MSG-4 can provide full-disk images every 15 minutes. SEVIRI has twelve spectral channels, of which eight are in the infrared. The spatial resolution of the infrared channels is 3 km. The SEVIRI level 1.5 image data were acquired from the European Organisation for the Exploitation of Meteorological Satellites (EUMETSAT) Earth Observation portal. The SEVIRI level 1.5 data are geolocated and have had radiometric calibration applied. As the SEVIRI level 1.5 data include calibrated top-of-atmospheric radiances instead of BTs in each channel, each radiance measurement has been converted into BT according to Planck's equation [35].

2.5. MERRA-2 Data

Sea surface and vertical atmospheric data are needed to drive radiative transfer simulations of top-of-atmosphere BTs to convert those of ABI and SEVIRI into equivalent SLSTR BTs. As the reanalysis ocean surface and atmospheric fields are internally consistent [36], this study uses atmospheric state vectors from the NASA Modern-Era Retrospective Analysis for Research and Applications, version 2 (MERRA-2; [37]). The reanalysis datasets contain geolocated, geophysical variables, including SST_{skin} and air temperature and humidity at 72 standard pressure levels [38,39], these were used to characterize the atmospheric conditions under which the satellite measurements were made for the radiative transfer model simulations of the spectral radiance for each satellite radiometer measurement, and also to derive the formulas to convert the BTs.

2.6. RTTOV Simulation

The radiative transfer model used here is the computationally efficient Radiative Transfer for Tiros Operational Vertical (RTTOV [40]) with sea surface and atmospheric state taken from MERRA-2 reanalysis.

3. Methods

This study used three research areas to perform the comparative analysis of the SLSTR BTs and those measured by geostationary satellite radiometers (Table 3).

Table 3. Details of the SLSTR L1-B data used in this study.

Areas	for	Date	UTC Time
Eastern tropical North Atlantic Ocean	SLSTR with ABI	1 January 2020	Day: 15:21:14 PM Night: 02:55:20 AM
Mediterranean Sea	SLSTR with SEVIRI	23 December 2019	Day: 09:04:56 AM Night: 20:21:51 PM
Cross-covered region	SLSTR with SEVIRI and ABI	27 November 2019	Day: 12:09:44 AM Night: 00:36:20 AM

The first step was to match the SLSTR with ABI and SEVIRI data based on latitude and longitude. Due to the fact that the three instruments have different spatial resolutions, the matched data provide measurements at nearly the same location. We selected the nearest point with the spatial distance between the SLSTR and matched data less than 1 km, which is less than their spatial resolution (Table 2). The time differences between them are usually <5 minutes to mitigate the effects of temporal temperature changes. The satellite viewing geometry is different for each sensor, so to reduce the effect of atmospheric absorption and scattering on radiance measurements, the SLSTR satellite zenith angle is limited to within 45 degrees, then the SLSTR oblique view data will be excluded. Then, the SLSTR Bayesian cloud mask was applied to remove the cloud-contaminated pixels. Additionally, the corresponding ACSPO and SEVIRI cloud masks were used to ensure the clear-sky scenes for the ABI and SEVIRI measurements.

The next step in the analyses was to harmonize the BT measurements taken by each satellite radiometer to account for the relative spectral response functions (Figure 1). The successful harmonization of the BTs obtained from all satellite radiometers is important to this study. Wu, et al. [21] and Yu and Wu [14] assumed the BTs of AHI and Advanced Very High-Resolution Radiometer (AVHRR) at specific channels could be linearly expressed by other similar spectral channels such as VIIRS and MODIS. Wu, et al. [21] and Sohn, et al. [41] used a simple conversion function when comparing MODIS BTs with those of Multifunctional Transport Satellites (MTSAT) or AVHRR. However, they selected the pixels with almost the same viewing geometries, the differences of satellite viewing angle are lower than 50 degrees to reduce the uncertainties caused by different viewing geometries. We updated the conversion functions with the secant of satellite zenith angle terms with respect to the BT changes. Li, et al. [17] and many other investigators used the spectral band difference adjustments based on the NASA Langley Scanning Imaging Absorption Chartography (SCIAMACHY) tool [20]. However, the data flow from SCIAMACHY ended with the failure of Environmental Satellite (Envisat) in April 2012, well before the launch of the Sentinel-3S and the GOES 16 ABI, therefore we derived conversion functions based on radiative transfer simulations to convert the ABI and SEVIRI BTs into SLSTR equivalents:

$$BT_{\text{SLSTR equivalent}} = a \times BT_{\text{ABI or SEVIRI}} + b \times BT_{\text{SLSTR}} \times (\sec(\theta_{\text{SLSTR}}) - 1) + c \\ \times BT_{\text{ABI or SEVIRI}} \times (\sec(\theta_{\text{ABI or SEVIRI}}) - 1) + d$$

The coefficients a , b , c , and d were determined by regressions of the SLSTR BT and ABI/SEVIRI BT of each channel and each geographic area. BT is the BT, θ is the satellite zenith angle. In this study, all of the analyses are based on BTs.

The form of this equation was derived by simulating the spectra of the radiation leaving the top of the atmosphere using RTTOV radiative transfer modeling with the atmospheric state taken from MERRA-2 to derive the simulated satellite radiometer measurements. The SST, 2m air temperature and surface wind data were taken from the MERRA-2 inst1_2d_asm dataset, the three-dimensional air temperature and relative humidity were taken from the MERRA-2 inst3_3d_asm_Nv dataset. The harmonization process is completed across the entire swath of the SLSTR. Satellite zenith angles

were set between 0° to 45° to derive the sensitivity to viewing geometry. We did not include the aerosol or cloud effects in the simulations.

4. Results and Discussion

4.1. Eastern Tropical North Atlantic Ocean Region

The variabilities of the oceanographic and atmospheric conditions along the Gulf Stream have drawn a lot of attention for many years. The Florida Current causes complex SST variations as well as a strong atmospheric response in this region [42]. Inter-comparison of Sentinel-3A SLSTR and GOES-16 ABI in this region supports the regional studies of the Gulf Stream and Florida Current.

Selecting a granule with less cloud cover than many others, Figure 3 shows the SLSTR false color infrared image of this area on 1 January 2020, 15:21:14 Coordinated Universal Time (UTC) and the corresponding satellite zenith angles and solar zenith angles. Figures 4 and 5 show the comparison of the pixel-by-pixel matched near-coincident measurements between SLSTR and ABI. All of the ABI values have been converted to SLSTR equivalent BTs. Clearly, there is generally good agreement between all three bands from these scenes. The overall SLSTR BTs are higher in the S8 and S9 comparisons. For SLSTR S7 compared to ABI band 7, there is a negative bias near the Bahamas islands, the S7 band can be contaminated by sun light and there are residual clouds near this region. Figure 5 (third row) shows the histograms of the BT differences in three bands. Their distribution patterns are similar but with many peaks for SLSTR S9 with ABI band 15. Some larger discrepancies, shown in the SLSTR S9 with ABI 15 scatter plot and difference distribution, are caused by large SLSTR satellite zenith angles and cloud edges.

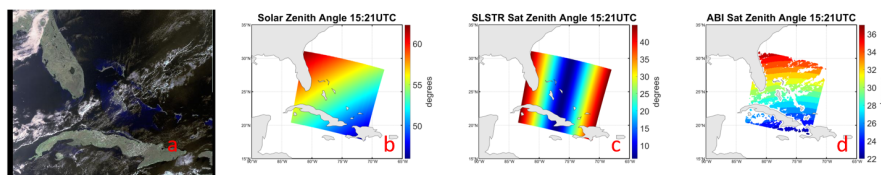


Figure 3. (a): SLSTR daytime false color infrared image of the eastern tropical North Atlantic Ocean coast on 1 January 2020, 15:21:14 UTC. (b): Solar zenith angles data at the same time. (c): Corresponding SLSTR satellite zenith angles. (d): Corresponding ABI satellite zenith angles, only the points with available ABI matched up pairs are shown.

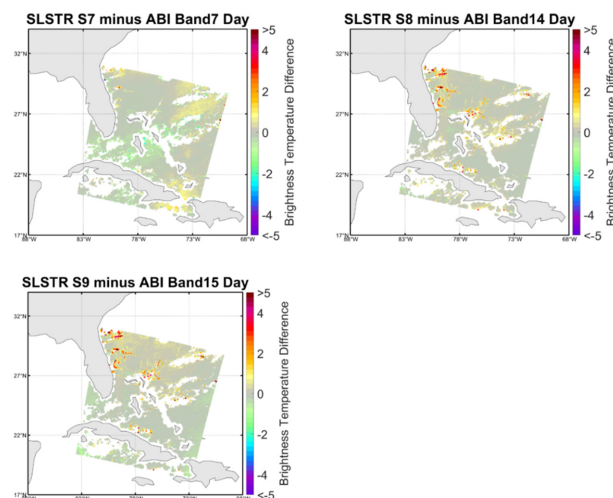


Figure 4. Distributions of the daytime brightness temperature (BT) differences between SLSTR and ABI in the eastern tropical North Atlantic Ocean of SLSTR S7 (top-left), S8 (top-right) and S9 (bottom-left). The colors indicate the SLSTR minus ABI equivalent BTs.

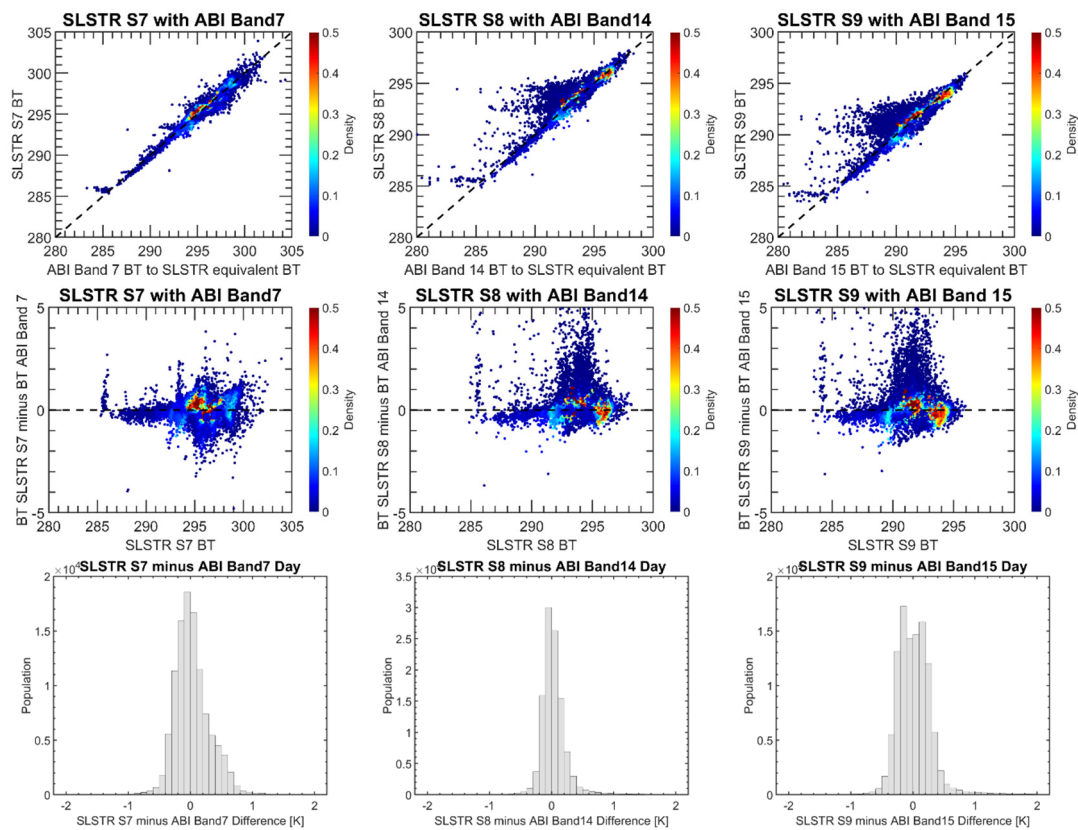


Figure 5. First row: scatter plots of the ABI equivalent BTs as a function of the SLSTR BTs of each channel pair. The colors show the density of the data according to the scale on the right. Second row: scatter plots of the SLSTR minus ABI BTs as a function of the SLSTR BT. Third row: histograms of the SLSTR minus ABI BTs. All of the ABI BTs indicate the transferred SLSTR-equivalent BTs. The BTs are divided into 0.5 K intervals. The density shows the number of matched points within 0.2 K times 0.2 K BT cells divided by the maximum number.

The nighttime false color infrared image is shown in Figure 6. There is a dense cloud cover. Figures 7 and 8 display the nighttime SLSTR BT versus equivalent BTs of ABI. The results of overall comparisons of the nighttime BTs are in better agreement with equivalent BTs than those of daytime.

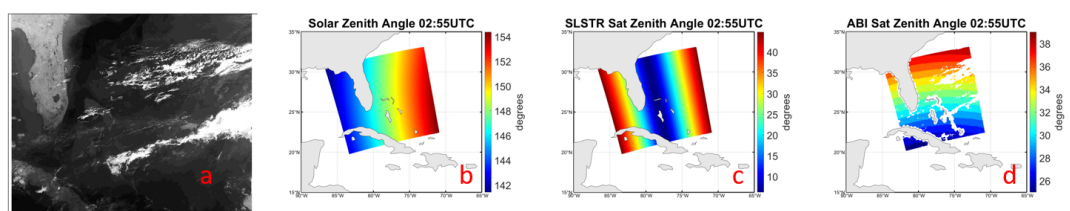


Figure 6. (a): SLSTR nighttime false color infrared image of the eastern tropical North Atlantic Ocean coast region on 1 January 2020, 02:55:20 UTC. (b): Solar zenith angles at the same time. (c): Corresponding SLSTR satellite zenith angles. (d): Corresponding ABI satellite zenith angles, only the points with available ABI matched up pairs are shown.

From the geographical distribution of BT differences corresponding to the matching and selection criteria (Figure 7), there is an overall positive bias when comparing the matched SLSTR and equivalent ABI BTs. The dashed lines in the panels in the first row of Figure 8 represent the one-to-one relationship, showing that for SLSTR bands S8 and S9, the BTs < 290 K deviate from the one-to-one lines. These results are consistent with other SLSTR BT comparisons, such as by Shrestha, et al. [43] who also found

such discrepancies at the lower SLSTR BTs when compared with those of MODIS. Here, this result may come from the residual contamination at cloud edges and by thin ice clouds, since their BTs are normally lower than those of the sea surface. Although no matchup pairs used to derive the ABI to SLSTR transfer functions are selected with the satellite zenith angle $> 45^\circ$ in this study, the difference distributions based on the selected granule show discrepancies with large viewing angles in S8 and S9 spectral channels. Figure 8 (third row) illustrates the histograms of the BT difference of SLSTR minus ABI during nighttime, which indicates the close similarity of the skewed distributions. Table 4 summarizes the statistics of the SLSTR BTs minus ABI equivalent BTs in this region, the averaged BT differences are on the order of -0.035 K to 0.079 K with the S7 band comparisons having the minimum average difference.

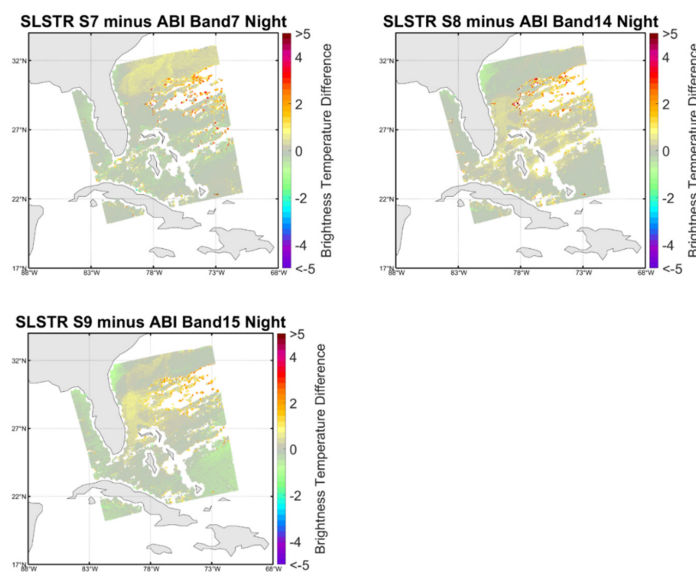


Figure 7. As shown in Figure 4, but for nighttime.

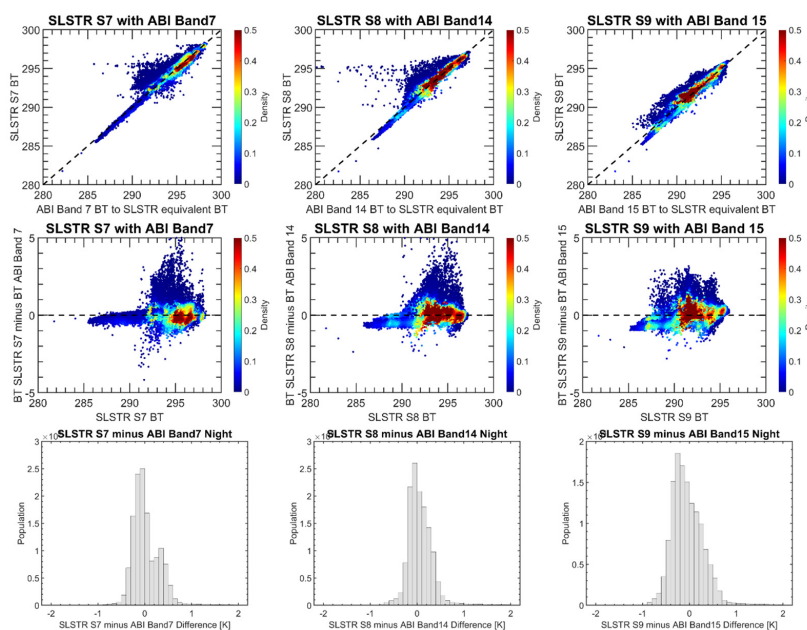


Figure 8. As shown in Figure 5, but for nighttime.

Table 4. Statistics of SLSTR BTs minus ABI equivalent BTs in eastern tropical North Atlantic Ocean. STD: standard deviation. RSD: robust standard deviation.

Eastern Tropical North Atlantic Ocean	Day/Night	Band (SLSTR)	Mean (K)	Median (K)	STD (K)	RSD (K)
SLSTR vs ABI	Day	S7	0.028	−0.005	0.296	0.248
		S8	0.054	0.008	0.326	0.145
		S9	0.042	0.006	0.401	0.260
	Night	S7	0.039	−0.033	0.360	0.281
		S8	0.079	0.028	0.383	0.230
		S9	−0.035	−0.088	0.360	0.330

4.2. Mediterranean Sea Region

As the largest semi-enclosed sea in the world, the Mediterranean Sea has highly specific oceanic characteristics. The SST diurnal cycles in the Mediterranean Sea are more frequent than global regions [44], which can cause marked SST changes. Several studies have estimated the heat budget and their relations to the SST diurnal cycle [45,46]. Satellite measurements can provide high-quality synoptic datasets to study the Mediterranean Sea heat budget, accurate knowledge of their performance is crucial for such research. Figure 9a gives the daytime false color infrared image and satellite geometry data on 23 December 2019, 09:04:56 UTC—the reason for choosing this time is that there is less cloud cover compared to other days.

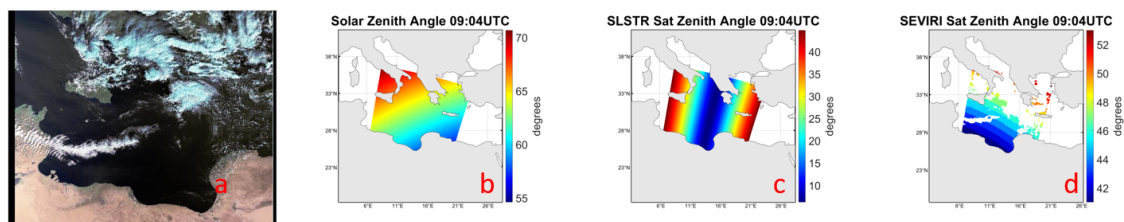


Figure 9. (a): SLSTR daytime false color infrared image of the Mediterranean Sea region on 23 December 2019, 09:04:56 UTC. (b): Solar zenith angles data at the same time. (c): Corresponding SLSTR satellite zenith angles. (d): Corresponding SEVIRI satellite zenith angles, only the points with available SEVIRI matched up pairs are shown.

Results of the comparisons in Figures 10 and 11 indicate that for most of the matched points (with high density at the scatter plots), SLSTR BTs agree well with SEVIRI data for S8 and S9 bands, while SLSTR S7 generally has larger differences with SEVIRI band 4 during the daytime due to solar effects. The fact that SLSTR S8 and S9 bands are biased warm may suggest there is residual cloud contamination in the SEVIRI in the Mediterranean Sea region. The SLSTR and SEVIRI cloud masks should be consistent with each other; however, there are large differences near cloud edges, and the difference in viewing angles to the cloud edge causes parallax, which may contribute to these differences.

The most apparent outliers within these channels belong to S7 with large scattering angles of solar radiation and large satellite zenith angles.

Visual inspection of the SLSTR nighttime false color infrared image (Figure 12a) confirms that the cloud edges are the leading cause of the significant warm bias between them. Although the matchup criteria have removed most of the pairs with cloud cover, some of the SEVIRI scenes still have low BTs probably due to the cloud emission instead of from the sea surface.

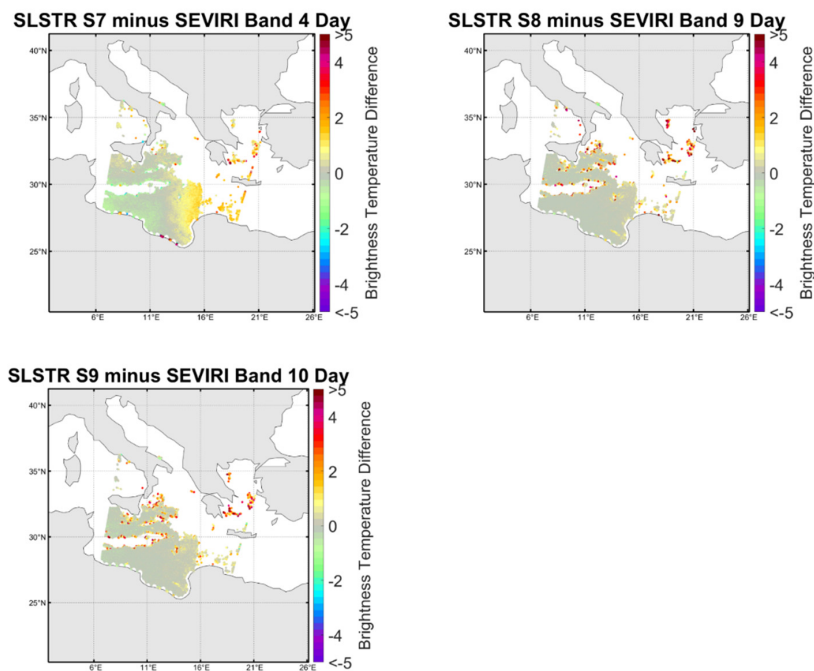


Figure 10. Distributions of the daytime BT differences between SLSTR and SEVIRI in the Mediterranean Sea region of SLSTR S7 (top-left), S8 (top-right) and S9 (bottom-left). The colors indicate the SLSTR minus SEVIRI equivalent BTs.

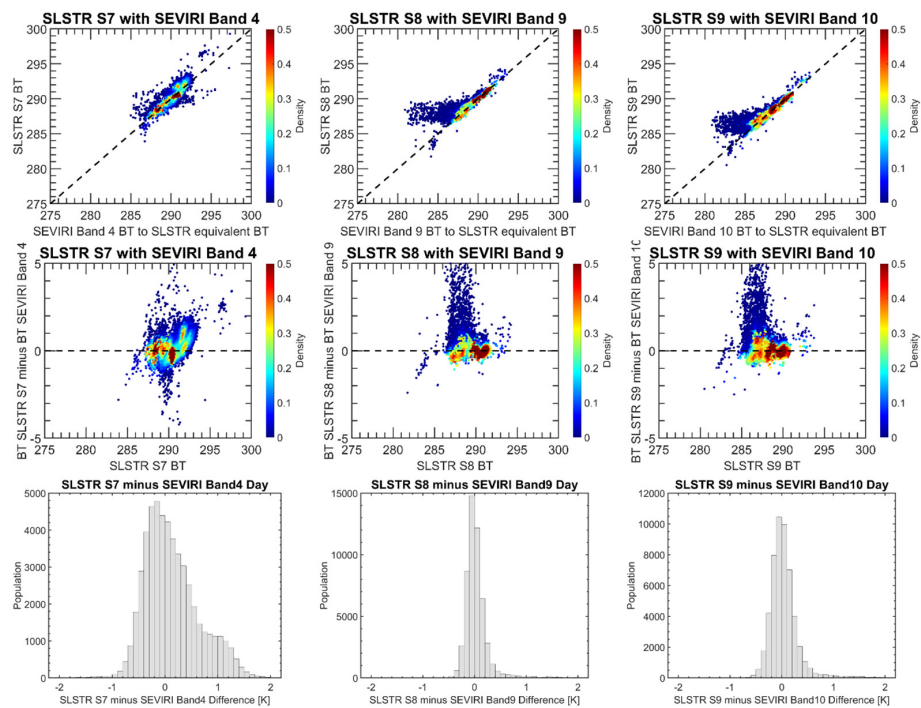


Figure 11. First row: scatter plot of the SLSTR BTs with SEVIRI equivalent BTs of each channel pair. The colors show the density of the data according to the right scale. Second row: scatter plot of the SLSTR BT with SLSTR minus SEVIRI BT of each channel pair. Third row: histograms of the BT differences of SLSTR minus SEVIRI for each channel pair. All of the SEVIRI BTs indicate the transferred SLSTR-equivalent BTs. The BTs are divided into 0.5 K intervals.

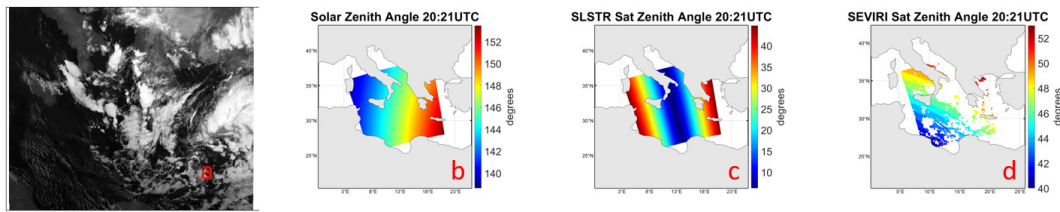


Figure 12. (a): SLSTR nighttime false color infrared image of the Mediterranean Sea region on 23 December 2019, 20:21:51 UTC. (b): Solar zenith angles at the same time. (c): Corresponding SLSTR satellite zenith angles. (d): Corresponding SEVIRI satellite zenith angles, only the points with available SEVIRI matched up pairs are shown.

Shown in Figures 13 and 14 are results of the SLSTR and SEVIRI comparison during nighttime. All of the results in these three channels display significant discrepancies at 280–285 K. The most likely distributions of these points with relatively large discrepancies are near coastal regions through visual inspection of Figure 13. Figure 14 (third row) shows the histograms of the BT differences. Each channel of them exhibits very similar difference distributions. Table 5 summarizes the statistics of the SLSTR BTs minus SEVIRI equivalent BTs in the Mediterranean Sea region, the averaged BT differences are over 0.1 K, which is larger than for other regions examined, which may be due to increased number of comparisons indicating cloud-edge effects.

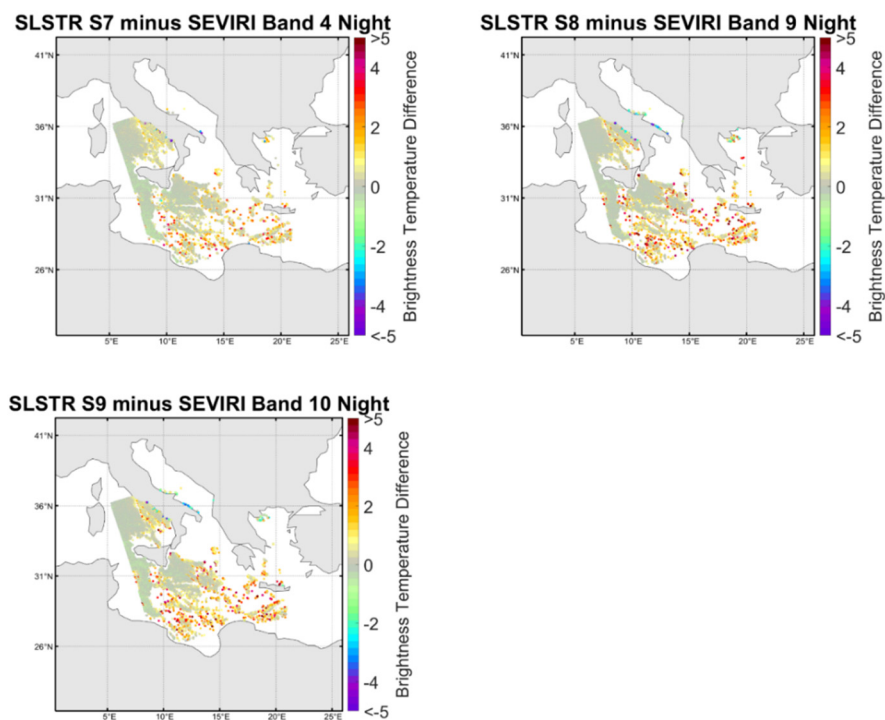


Figure 13. As shown in Figure 10, but for nighttime.

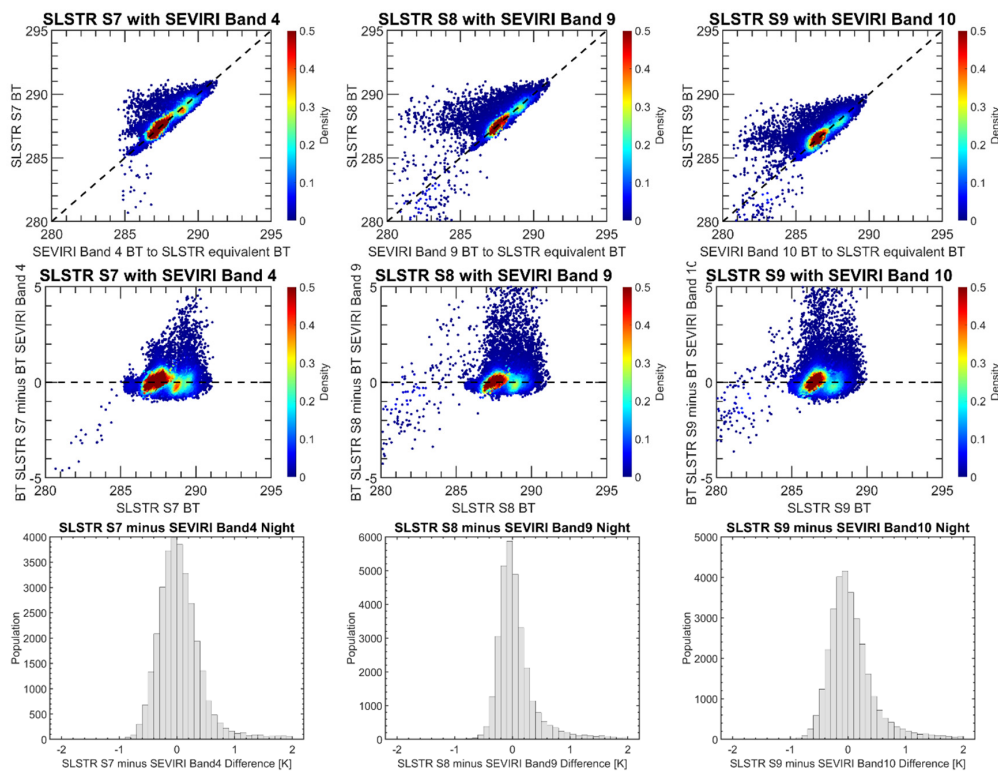


Figure 14. As shown in Figure 11, but for nighttime.

Table 5. Statistics of SLSTR BTs minus SEVIRI equivalent BTs in the Mediterranean Sea area.

Mediterranean Sea	Day/Night	Band (SLSTR)	Mean (K)	Median (K)	STD (K)	RSD (K)
SLSTR vs SEVIRI	Day	S7	0.133	0.045	0.544	0.493
		S8	0.067	−0.005	0.454	0.143
		S9	0.073	0.008	0.440	0.198
	Night	S7	0.077	0.012	0.480	0.320
		S8	0.143	−0.003	0.674	0.240
		S9	0.124	−0.003	0.644	0.328

4.3. Cross-Covered Region

GOES-16 is located above 75.2°W and MSG-4 is located above 0°W; thus, the areas near 37.5°W are under the coverage of three satellites when Sentinel-3A underlies the geostationary satellites. After checking SLSTR true color images, we found this area always includes large amounts of cloud. For this case, two granules of Sentinel-3A SLSTR data from 27 November 2019 are selected to perform the inter-comparison of the three radiometers because of the relatively small cloud coverage compared to other days. The inter-comparison of the thermal emissive bands over this region can further show their performance under the same conditions.

The false color infrared image and satellite geometry data are given in Figure 15. It is clear that the daytime SLSTR image has solar contamination as the area in the right of Figure 15a shows a sun-glitter pattern. There is also a thin cloud cover over this region on 27 November 2019, 12:09 UTC. As the SLSTR S7 near 3.74 μm usually suffers from sunlight contamination during daytime and there is a clear sun-glitter patch in the scene, the SLSTR S8 and S9 BTs are preliminarily evaluated with the corresponding ABI and SEVIRI BTs.

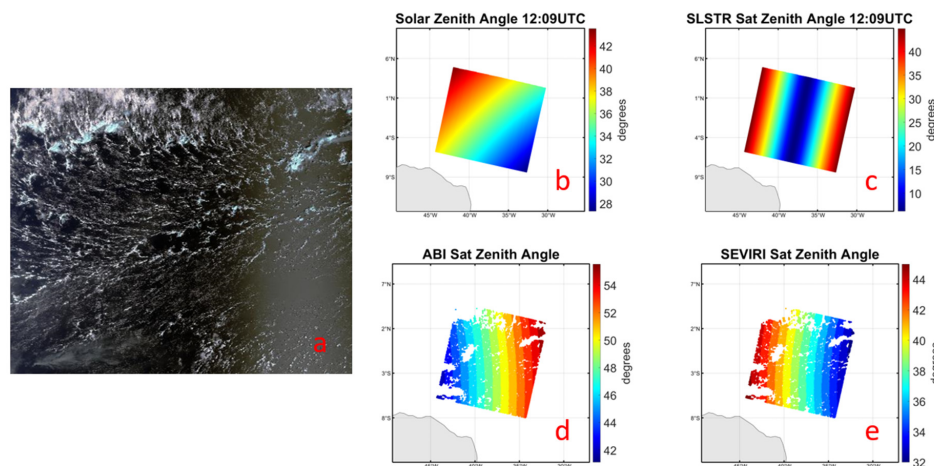


Figure 15. (a): SLSTR daytime false color infrared image of the cross-covered region on 27 November 2019, 12:09 UTC. (b): Solar zenith angles data at the same time. Corresponding SLSTR (c), ABI (d), SEVIRI (e) satellite zenith angles data.

The cross-comparisons of these three radiometers in this region are limited to SLSTR satellite zenith angles less than 20 degrees as this reduces the range of zenith angle differences to the geostationary satellites. Figure 16 shows the geographical distribution of the daytime BT differences. In comparison to the two infrared channels of SEVIRI, the ABI channels 14 and 15 (shown in the first row of Figure 17) show much larger discrepancies at lower SLSTR BTs, indicating a significant underestimate of BT. Most of the matchup pairs with positive discrepancies at the first row are near the cloud edge, and larger positive discrepancies occur at lower SLSTR BTs, as shown in the second row of Figure 17. All of these discrepancies can also be addressed in the third row, which shows the histograms of the daytime BT differences in three bands.

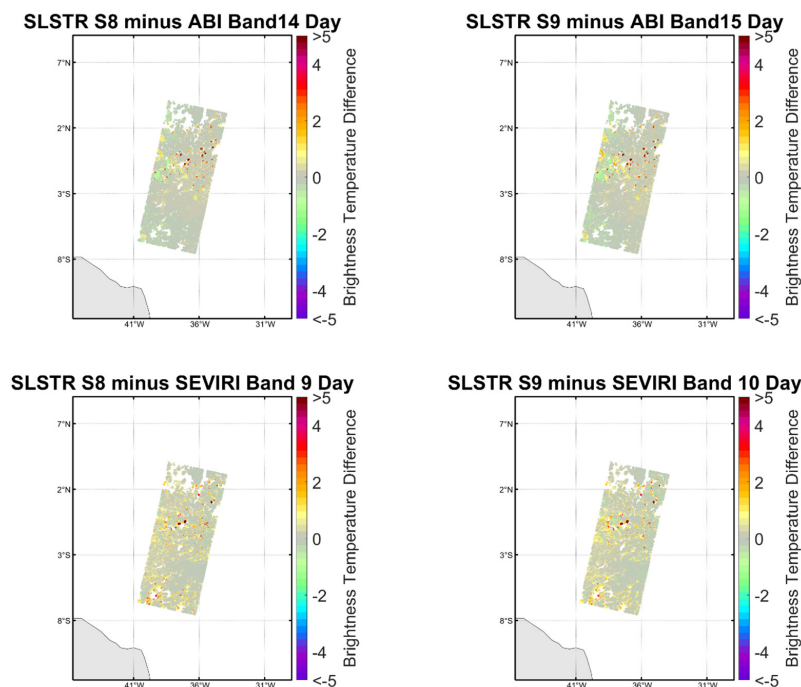


Figure 16. First row: distributions of the daytime BT difference between SLSTR and ABI in the cross-covered region on 27 November 2019, 12:09 UTC. The color indicates the SLSTR minus SEVIRI equivalent BT. Second row: corresponding BT difference distributions between SLSTR and SEVIRI.

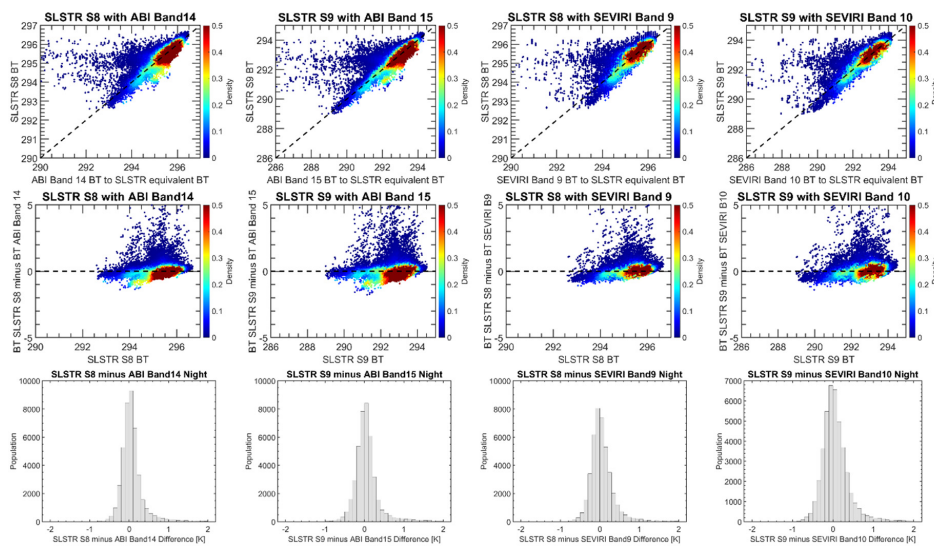


Figure 17. First row: scatter plots of the ABI/SEVIRI equivalent BTs as a function of the SLSTR BTs of each channel pair. The colors show the density of the data according to the scale on the right. Second row: scatter plots of the SLSTR minus ABI/SEVIRI BTs as a function of the SLSTR BT. Third row: histograms of the SLSTR minus ABI/SEVIRI BTs. All of the ABI/SEVIRI BTs indicate the transferred SLSTR-equivalent BTs. The BTs are divided into 0.5 K intervals.

The nighttime false color infrared image and satellite view geometries are shown in Figure 18. Figures 19 and 20 show the nighttime comparisons between SLSTR, ABI and SEVIRI. Figure 19 shows the geographic distributions of the BT differences in two bands. As for the eastern tropical North Atlantic Ocean region, the nighttime comparisons show better agreement compared to daytime. The significant positive discrepancies can also be found at the image near the cloud edge. Strong linear relationships between SLSTR and ABI/SEVIRI can be found at most of the matched-up points, as indicated by the first row of Figure 20. However, the overall fitting slopes of high density-points do not agree well with the one-to-one black line. The discrepancies may suggest that the conversion functions have larger uncertainties over this region. Possible reasons are greater water vapor concentrations and large ABI/SEVIRI satellite zenith angles.

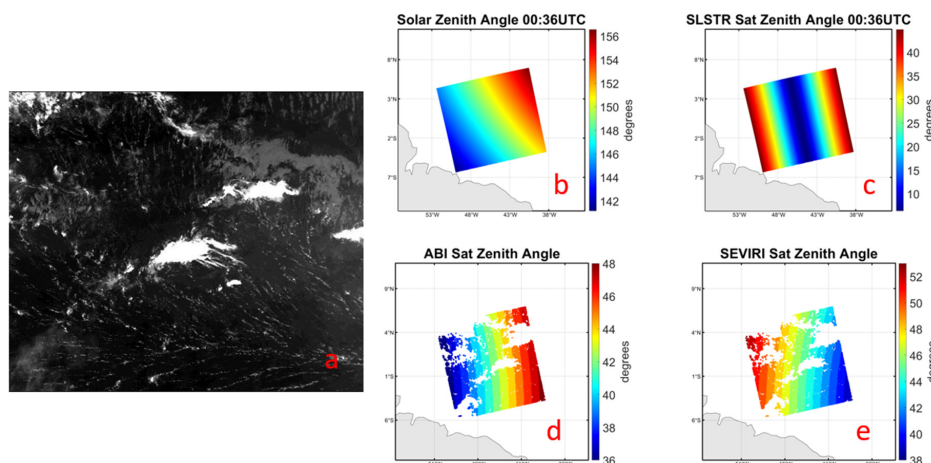


Figure 18. (a): SLSTR nighttime false color infrared image of the cross-covered region on 27 November 2019, 00:36 UTC. (b): Solar zenith angles data at the same time. Corresponding SLSTR (c), ABI (d), SEVIRI (e) satellite zenith angles data.

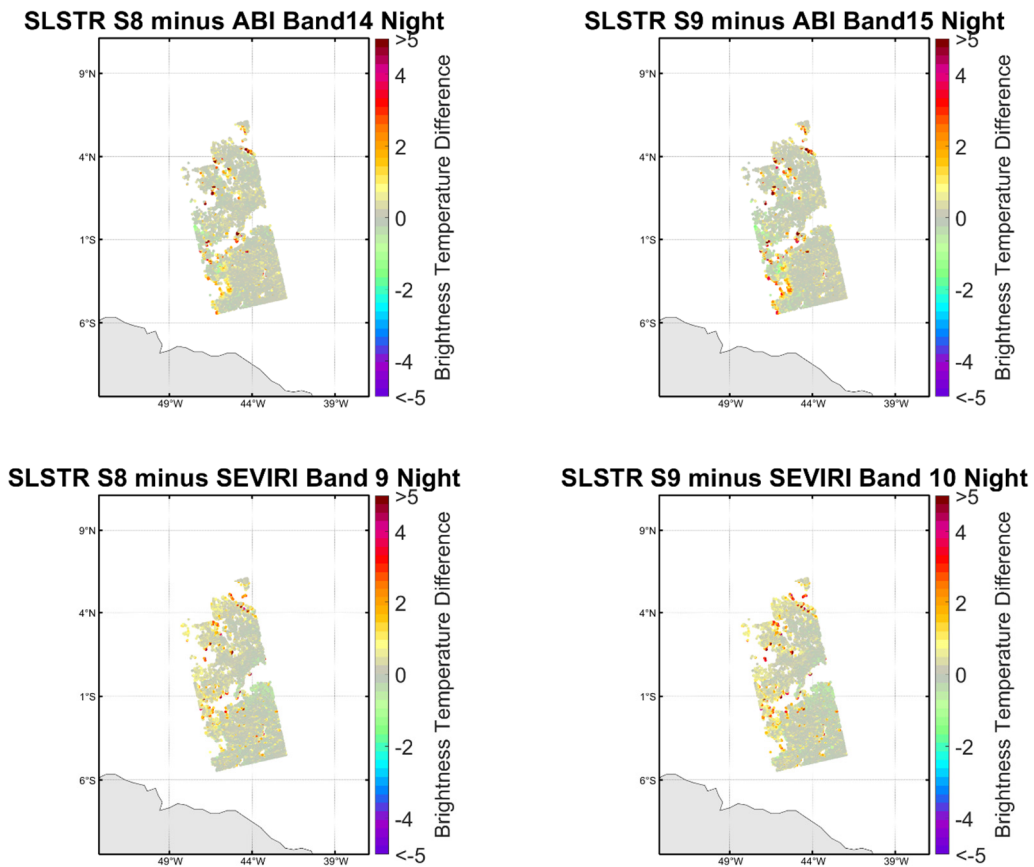


Figure 19. As shown in Figure 16, but for nighttime.

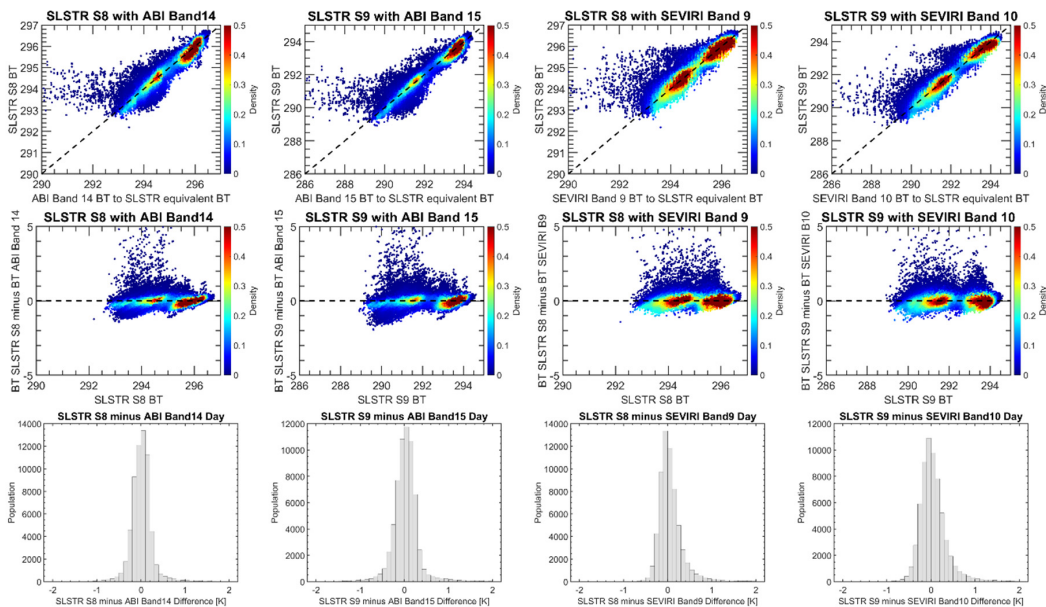


Figure 20. As shown in Figure 17, but for nighttime.

Table 6 shows the statistics of the SLSTR BTs minus ABI/SEVIRI equivalent BTs. The average BT differences are on the order of 0.1 K. Daytime comparisons are better than at nighttime in terms of the average difference and standard deviations. The standard deviations of SLSTR vs ABI are higher than SLSTR vs SEVIRI. The SLSTR S9 band comparisons have larger differences than the S8 band comparisons.

Table 6. Statistics of SLSTR BTs minus ABI/SEVIRI equivalent BTs.

Cross-Covered Region	Day/Night	Band (SLSTR)	Mean (K)	Median (K)	STD (K)	RSD (K)
SLSTR vs ABI	Day	S8	0.035	0.013	0.452	0.184
		S9	0.056	0.030	0.516	0.211
	Night	S8	0.128	0.036	0.891	0.186
		S9	0.143	0.025	1.084	0.207
SLSTR vs SEVIRI	Day	S8	0.087	0.018	0.450	0.202
		S9	0.072	0.010	0.467	0.241
	Night	S8	0.084	0.014	0.465	0.224
		S9	0.105	0.024	0.549	0.265

5. Conclusions

With the significant improvements in design, SLSTRs onboard the Sentinel-3A series of satellites provide observational data in nine visible to infrared bands. Good absolute calibration is required for the accurate derivation of SST_{skin} from radiance measurements, which is achieved by using two onboard blackbodies. Even so, external comparisons of the SLSTR BTs with those of other satellite radiometers are extremely important to ensure the stability and continuity of the long-term satellite climate-related data products, which require the combination of measurements from multiple satellite radiometers, including different designs.

Among the SLSTR nine spectral channels in the 0.554–12.022 μm wavelength spectral range, bands S7 (3.74 μm), S8 (10.95 μm), and S9 (12.00 μm) are used for deriving the SST_{skin} . Here, we compared the BTs of these three SLSTR thermal emission bands with those from geostationary satellite radiometers.

Pixel-by-pixel collocated BTs from SLSTR, ABI, and SEVIRI were used together with their cloud masks to select clear-sky measurements. Empirical regression formulas derived from simulated top-of-atmosphere radiance spectra using the relative spectral response functions of each band were used to convert ABI and SEVIRI BTs to SLSTR-equivalent values, taking into account the satellite zenith angle. The results indicate that SLSTR thermal emissive bands S7, S8 and S9 are comparably well-calibrated as the corresponding ABI and SEVIRI bands, except for S7 bands, which suffer from sunlight contamination during daytime. The measurements from the different satellite radiometers can be combined within the accuracy limits shown in Tables 4–6. Given the occurrence of outliers in the distributions of the BT differences, the robust standard deviation is a better measure of the correspondence of the measurements of the different radiometers. The main differences are due to the residual cloud edges and coast effects, probably land-mask effects, while the other disagreements may be due to different viewing angles and solar contamination of measurements in the mid-infrared atmospheric transmission window. However, it is apparent that the cloud-screening algorithms for all sensors are not identifying all cases of cloud contamination.

It should be noted that the coefficients in the equation to derive SLSTR-equivalent BTs for the geostationary satellite data are dependent on each scene, as a result of the limited ranges of SST and atmospheric conditions in each. Conversion equations applicable to larger areas with greater variability and different times require additional terms, possibly including additional variables, such as the water vapor amount.

Author Contributions: Conceptualization, methodology, software, validation, data curation, writing—original draft preparation, funding acquisition: B.L.; supervision, writing—review and editing, visualization, project administration, funding acquisition: P.J.M. All authors have read and agreed to the published version of the manuscript.

Funding: This research was funded by Rosenstiel School of Marine and Atmospheric Science (RSMAS) Mary Roche endowed Fellowship, EUMETSAT Copernicus Scholarships, Future Investigators in NASA Earth and

Space Science and Technology (FINESST) Program (grant # 80NSSC19K1326), NASA US Participating Investigator Program (grant # NNX17AL69G).

Acknowledgments: This work has benefited from discussions with colleagues at RSMAS.

Conflicts of Interest: The authors declare no conflict of interest.

References

- Bentamy, A.; Piollé, J.F.; Grouazel, A.; Danielson, R.; Gulev, S.; Paul, F.; Azelmat, H.; Mathieu, P.P.; von Schuckmann, K.; Sathyendranath, S.; et al. Review and assessment of latent and sensible heat flux accuracy over the global oceans. *Remote Sens. Environ.* **2017**, *201*, 196–218. [[CrossRef](#)]
- Minnett, P.J.; Alvera-Azcárate, A.; Chin, T.M.; Corlett, G.K.; Gentemann, C.L.; Karagali, I.; Li, X.; Marsouin, A.; Marullo, S.; Maturi, E.; et al. Half a century of satellite remote sensing of sea-surface temperature. *Remote Sens. Environ.* **2019**, *233*, 111366. [[CrossRef](#)]
- Luo, B.; Minnett, P.J.; Szczodrak, M.; Kilpatrick, K.; Izaguirre, M. Validation of Sentinel-3A SLSTR derived Sea-Surface Skin Temperatures with those of the shipborne M-AERI. *Remote Sens. Environ.* **2020**, *244*, 111826. [[CrossRef](#)]
- Donlon, C.; Berruti, B.; Buongiorno, A.; Ferreira, M.H.; Féménias, P.; Frerick, J.; Goryl, P.; Klein, U.; Laur, H.; Mavrocordatos, C.; et al. The Global Monitoring for Environment and Security (GMES) Sentinel-3 mission. *Remote Sens. Environ.* **2012**, *120*, 37–57. [[CrossRef](#)]
- Coppo, P.; Ricciarelli, B.; Brandani, F.; Delderfield, J.; Ferlet, M.; Mutlow, C.; Munro, G.; Nightingale, T.; Smith, D.; Bianchi, S.; et al. SLSTR: A high accuracy dual scan temperature radiometer for sea and land surface monitoring from space. *J. Mod. Opt.* **2010**, *57*, 1815–1830. [[CrossRef](#)]
- Mutlow, C.T.; Llewellyn-Jones, D.T.; Závody, A.M.; Barton, I.J. Sea-surface temperature measurements by the Along-Track Scanning Radiometer (ATSR) on ESA's ERS-1 Satellite—Early results. *J. Geophys. Res.* **1994**, *99*, 22575–22588. [[CrossRef](#)]
- Llewellyn-Jones, D.; Remedios, J. The Advanced Along Track Scanning Radiometer (AATSR) and its predecessors ATSR-1 and ATSR-2: An introduction to the special issue. *Remote Sens. Environ.* **2012**, *116*, 1–3. [[CrossRef](#)]
- Smith, D.L.; Nightingale, T.J.; Mortimer, H.; Middleton, K.; Edeson, R.; Cox, C.V.; Mutlow, C.T.; Maddison, B.J.; Coppo, P. Calibration approach and plan for the sea and land surface temperature radiometer. *J. Appl. Remote Sens.* **2014**, *8*, 084980. [[CrossRef](#)]
- Smith, D.; Barillot, M.; Bianchi, S.; Brandani, F.; Coppo, P.; Etxaluze, M.; Frerick, J.; Kirschstein, S.; Lee, A.; Maddison, B. Sentinel-3A/B SLSTR pre-launch calibration of the thermal infrared channels. *Remote Sens.* **2020**, *12*, 2510. [[CrossRef](#)]
- Schmit, T.J.; Gunshor, M.M.; Menzel, W.P.; Gurka, J.J.; Li, J.; Bachmeier, A.S. Introducing the Next-Generation Advanced Baseline Imager on GOES-R. *Bull. Am. Meteorol. Soc.* **2005**, *86*, 1079–1096. [[CrossRef](#)]
- Aminou, D.M.A. MSG's SEVIRI instrument. *ESA Bull.* **2002**, *11*, 15–17.
- Bessho, K.; Date, K.; Hayashi, M.; Ikeda, A.; Imai, T.; Inoue, H.; Kumagai, Y.; Miyakawa, T.; Murata, H.; Ohno, T. An introduction to Himawari-8/9—Japan's new-generation geostationary meteorological satellites. *J. Meteorol. Soc. Jpn. Ser. II* **2016**, *94*, 151–183. [[CrossRef](#)]
- Minnett, P.J.; Evans, R.H.; Podestá, G.P.; Kilpatrick, K.A. Sea-surface temperature from Suomi-NPP VIIRS: Algorithm development and uncertainty estimation. In Proceedings of the SPIE 9111, Ocean Sensing and Monitoring VI, 91110C, Baltimore, MD, USA, 23 May 2014; p. 91110C.
- Yu, F.; Wu, X. Radiometric inter-calibration between Himawari-8 AHI and S-NPP VIIRS for the solar reflective bands. *Remote Sens.* **2016**, *8*, 165. [[CrossRef](#)]
- Liang, X.; Ignatov, A.; Kramar, M.; Yu, F. Preliminary Inter-Comparison between AHI, VIIRS and MODIS Clear-Sky Ocean Radiances for Accurate SST Retrievals. *Remote Sens.* **2016**, *8*, 203. [[CrossRef](#)]
- Salomonson, V.V.; Barnes, W.L.; Maymon, P.W.; Montgomery, H.E.; Ostrow, H. MODIS: Advanced facility instrument for studies of the earth as a system. *IEEE Trans. Geosci. Remote Sens.* **1989**, *27*, 145–153. [[CrossRef](#)]
- Li, Y.; Wu, A.; Xiong, X. Inter-Comparison of S-NPP VIIRS and Aqua MODIS Thermal Emissive Bands Using Hyperspectral Infrared Sounder Measurements as a Transfer Reference. *Remote Sens.* **2016**, *8*, 72. [[CrossRef](#)]
- Wang, L.; Cao, C.; Ciren, P. Assessing NOAA-16 HIRS radiance accuracy using simultaneous nadir overpass observations from AIRS. *J. Atmos. Ocean. Technol.* **2007**, *24*, 1546–1561. [[CrossRef](#)]

19. Wang, L.; Tremblay, D.; Zhang, B.; Han, Y. Fast and accurate collocation of the visible infrared imaging radiometer suite measurements with cross-track infrared sounder. *Remote Sens.* **2016**, *8*, 76. [[CrossRef](#)]
20. Scarino, B.R.; Doelling, D.R.; Minnis, P.; Gopalan, A.; Chee, T.; Bhatt, R.; Lukashin, C.; Haney, C. A web-based tool for calculating spectral band difference adjustment factors derived from SCIAMACHY hyperspectral data. *IEEE Trans. Geosci. Remote Sens.* **2016**, *54*, 2529–2542. [[CrossRef](#)]
21. Wu, A.; Cao, C.; Xiong, X. Intercomparison of the 11-and 12-um bands of Terra and Aqua MODIS using NOAA-17 AVHRR. In *Earth Observing Systems VIII, Proceedings of the Optical Science and Technology, SPIE's 48th Annual Meeting, San Diego, CA, USA, 3–8 August 2003*; International Society for Optics and Photonics: Bellingham, WA, USA, 2003; Volume 5151, pp. 384–394.
22. Merchant, C. SENTINEL-3 Sea Surface Temperature (SLSTR) Algorithm Theoretical Basis Document. Available online: https://www.eumetsat.int/website/wcm/idc/idcplg?IdcService=GET_FILE&dDocName=PDF_S3_L2_ATBD_SLSTR_SST&RevisionSelectionMethod=LatestReleased&Rendition=Web (accessed on 1 August 2020).
23. Ignatov, A. GOES-R Advanced Baseline Imager (ABI) Algorithm Theoretical Basis Document for Sea Surface Temperature. 2010. Available online: https://www.star.nesdis.noaa.gov/goesr/documents/ATBDs/Baseline/ATBD_GOES-R_SST-v2.0_Aug2010.pdf:NOAA/NESDIS/STAR (accessed on 1 August 2020).
24. Merchant, C.J.; Le Borgne, P.; Roquet, H.; Marsouin, A. Sea surface temperature from a geostationary satellite by optimal estimation. *Remote Sens. Environ.* **2009**, *113*, 445–457. [[CrossRef](#)]
25. Romaguera, M.; Sobrino, J.A.; Olesen, F.S. Estimation of sea surface temperature from SEVIRI data: Algorithm testing and comparison with AVHRR products. *Int. J. Remote Sens.* **2006**, *27*, 5081–5086. [[CrossRef](#)]
26. Heidinger, A. ABI cloud mask NOAA NESDIS STAR Algorithm Theoretical Basis Doc 2011. Available online: https://www.star.nesdis.noaa.gov/goesr/docs/ATBD/Cloud_Mask.pdf (accessed on 1 August 2020).
27. Walton, C.; Pichel, W.; Sapper, J.; May, D. The development and operational application of nonlinear algorithms for the measurement of sea surface temperatures with the NOAA polar-orbiting environmental satellites. *J. Geophys. Res. Ocean.* **1998**, *103*, 27999–28012. [[CrossRef](#)]
28. Kilpatrick, K.A.; Podestá, G.; Walsh, S.; Williams, E.; Halliwell, V.; Szczodrak, M.; Brown, O.B.; Minnett, P.J.; Evans, R. A decade of sea surface temperature from MODIS. *Remote Sens. Environ.* **2015**, *165*, 27–41. [[CrossRef](#)]
29. Good, E.J.; Kong, X.; Embury, O.; Merchant, C.J.; Remedios, J.J. An infrared desert dust index for the Along-Track Scanning Radiometers. *Remote Sens. Environ.* **2012**, *116*, 159–176. [[CrossRef](#)]
30. Merchant, C.J.; Embury, O.; Le Borgne, P.; Bellec, B. Saharan dust in nighttime thermal imagery: Detection and reduction of related biases in retrieved sea surface temperature. *Remote Sens. Environ.* **2006**, *104*, 15–30. [[CrossRef](#)]
31. Luo, B.; Minnett, P.J.; Gentemann, C.; Szczodrak, G. Improving satellite retrieved night-time infrared sea surface temperatures in aerosol contaminated regions. *Remote Sens. Environ.* **2019**, *223*, 8–20. [[CrossRef](#)]
32. Merchant, C.J.; Harris, A.R.; Murray, J.; Zavody, A.M. Toward the elimination of bias in satellite retrievals of skin sea surface temperature. 1: Theory. modelling and inter-algorithm comparison. *J. Geophys. Res.* **1999**, *104*, 23565–23578. [[CrossRef](#)]
33. Minnett, P.J.; Knuteson, R.O.; Best, F.A.; Osborne, B.J.; Hanafin, J.A.; Brown, O.B. The Marine-Atmospheric Emitted Radiance Interferometer (M-AERI), a high-accuracy, sea-going infrared spectroradiometer. *J. Atmos. Ocean. Technol.* **2001**, *18*, 994–1013. [[CrossRef](#)]
34. Petrenko, B.; Ignatov, A.; Kihai, Y.; Heidinger, A. Clear-Sky Mask for the Advanced Clear-Sky Processor for Oceans. *J. Atmos. Ocean. Technol.* **2010**, *27*, 1609–1623. [[CrossRef](#)]
35. Tjemkes, S.A. On the Conversion from Radiances to Equivalent Brightness Temperatures. 2005. Available online: http://www.eumetsat.int/groups/ops/documents/document/pdf_msg_seviri_rad2bright.pdf (accessed on 1 August 2020).
36. Luo, B.; Minnett, P. Evaluation of the ERA5 Sea Surface Skin Temperature with Remotely-Sensed Shipborne Marine-Atmospheric Emitted Radiance Interferometer Data. *Remote Sens.* **2020**, *12*, 1873. [[CrossRef](#)]
37. Gelaro, R.; McCarty, W.; Suárez, M.J.; Todling, R.; Molod, A.; Takacs, L.; Randles, C.A.; Darmenov, A.; Bosilovich, M.G.; Reichle, R.; et al. The Modern-Era Retrospective Analysis for Research and Applications, Version 2 (MERRA-2). *J. Clim.* **2017**, *30*, 5419–5454. [[CrossRef](#)] [[PubMed](#)]

38. Luo, B.; Minnett, P.J.; Szczodrak, M.; Nalli, N.R.; Morris, V.R. Accuracy assessment of MERRA-2 and ERA-Interim sea-surface temperature, air temperature and humidity profiles over the Atlantic Ocean using AEROSSE measurements. *J. Clim.* **2020**, *33*, 6889–6909. [[CrossRef](#)]
39. Bosilovich, M.G.; Santha, A.; Lawrence, C.; Richard, C.; Clara, D.; Ronald, G.; Robin, K.; Qing, L.; Andrea, M.; Peter, N.; et al. *MERRA-2: Initial Evaluation of the Climate*; NASA Goddard Space Flight Center: Greenbelt, MA, USA, 2015; p. 145.
40. Saunders, R.; Hocking, J.; Turner, E.; Rayer, P.; Rundle, D.; Brunel, P.; Vidot, J.; Roquet, P.; Matricardi, M.; Geer, A. An update on the RTTOV fast radiative transfer model (currently at version 12). *Geosci. Model Dev.* **2018**, *11*. [[CrossRef](#)]
41. Sohn, B.J.; Park, H.S.; Han, H.J.; Ahn, M.H. Evaluating the calibration of MTSAT-1R infrared channels using collocated Terra MODIS measurements. *Int. J. Remote Sens.* **2008**, *29*, 3033–3042. [[CrossRef](#)]
42. Minobe, S.; Miyashita, M.; Kuwano-Yoshida, A.; Tokinaga, H.; Xie, S.-P. Atmospheric response to the Gulf Stream: Seasonal variations. *J. Clim.* **2010**, *23*, 3699–3719. [[CrossRef](#)]
43. Shrestha, A.; Angal, A.; Xiong, X. Evaluation of MODIS and Sentinel-3 SLSTR thermal emissive bands calibration consistency using Dome C. In *Algorithms and Technologies for Multispectral, Hyperspectral, and Ultraspectral Imagery XXIV*; International Society for Optics and Photonics: Orlando, FL, USA, 2018; Volume 10644, p. 106441U.
44. Marullo, S.; Santoleri, R.; Ciani, D.; Le Borgne, P.; Péré, S.; Pinardi, N.; Tonani, M.; Nardone, G. Combining model and geostationary satellite data to reconstruct hourly SST field over the Mediterranean Sea. *Remote Sens. Environ.* **2014**, *146*, 11–23. [[CrossRef](#)]
45. Marullo, S.; Artale, V.; Santoleri, R. The SST Multidecadal Variability in the Atlantic–Mediterranean Region and Its Relation to AMO. *J. Clim.* **2011**, *24*, 4385–4401. [[CrossRef](#)]
46. Marullo, S.; Minnett, P.J.; Santoleri, R.; Tonani, M. The diurnal cycle of sea-surface temperature and estimation of the heat budget of the Mediterranean Sea. *J. Geophys. Res. Ocean.* **2016**, *121*, 8351–8367. [[CrossRef](#)]



© 2020 by the authors. Licensee MDPI, Basel, Switzerland. This article is an open access article distributed under the terms and conditions of the Creative Commons Attribution (CC BY) license (<http://creativecommons.org/licenses/by/4.0/>).